Journal of
Materials Chemistry A

PAPER

View Article Online
View Journal

Cite this: DOI: 10.1039/c9ta03503f

Enhanced thermoelectric performance of GeTe through *in situ* microdomain and Ge-vacancy control†

Khasim Saheb Bayikadi,[a] Raman Sankar, *[ab] Chien Ting Wu,[e] Chengliang Xia,[f] Yue Chen, [f] Li-Chyong Chen,[bd] Kuei-Hsien Chen *[bc] and Fang-Cheng Chou *[bd]

A highly reproducible sample preparation method for pure GeTe in a rhombohedral structure without converting to the cubic structure up to ~500 °C is reported to show control of the Ge-vacancy level and the corresponding herringbone-structured microdomains. The thermoelectric figure-of-merit (*ZT*) for GeTe powder could be raised from ~0.8 to 1.37 at high temperature (HT) near ~500 °C by tuning the Ge-vacancy level through the applied reversible *in situ* route, which made it highly controllable and reproducible. The enhanced *ZT* of GeTe was found to be strongly correlated with both its significantly increased Seebeck coefficient (~161 μV K^{-1} at 500 °C) and reduced thermal conductivity (~2.62 W m^{-1} K^{-1} at 500 °C) for a sample with nearly vacancy-free thicker herringbone-structured microdomains in the suppressed rhombohedral-to-cubic structure phase transformation. The microdomain and crystal structures were identified with HR-TEM (high-resolution transmission electron microscopy) and powder X-ray diffraction (XRD), while electron probe micro-analysis (EPMA) was used to confirm the stoichiometry changes of Ge : Te. Theoretical calculations for GeTe with various Ge-vacancy levels suggested that the Fermi level shifts toward the valence band as a function of increasing the Ge-vacancy level, which is consistent with the increased hole-type carrier concentration (*n*) and effective mass (*m**) deduced from the Hall measurements. The uniquely prepared sample of a near-vacancy-free GeTe in a rhombohedral structure at high temperature favoured an enhanced Seebeck coefficient in view of the converging L- and Σ-bands of the heavy effective mass at the Fermi level, while the high density domain boundaries for the domain of low carrier density were shown to reduce the total thermal conductivity effectively.

Received 2nd April 2019
Accepted 16th May 2019

DOI: 10.1039/c9ta03503f

rsc.li/materials-a

Introduction

The thermoelectric conversion efficiency of a material at specified temperature (T) is a measure of the synergetic organisation of its electrical conductivity (σ), Seebeck coefficient (S), and thermal conductivity ($\kappa = \kappa_{\rm ele} + \kappa_{\rm lat}$; $\kappa_{\rm ele}$ = electronic and $\kappa_{\rm lat}$ = lattice contributions), which leads to the indicator of thermoelectric performance as the figure-of-merit $ZT = S^2\sigma T/\kappa$. However, despite the momentous effort to simultaneously enhance the *ZT* of thermoelectric materials through raising the power factor ($S^2\sigma$) and reducing the thermal conductivity (κ), it remains a challenge with only marginal progress made so far.[1,2] For example, in order to enhance the power factor, strategies including band convergence,[3–6] energy filtering,[7,8] creating resonant energy levels,[9,10] and quantum confinement (size reduction) have been applied.[11] On the other hand, thermal conductivity reduction has been demonstrated successfully by means of point defects, nano-inclusions of secondary phases,[12–15] meso-scale boundaries,[13,14] bond anharmonicity,[16] and rattling modes.[17] Most importantly, even though a few sporadic reports have claimed record-high *ZT* values, the practical value of these findings has been hampered by their reproducibility, which has created many debatable studies in the literature.[16,18] No matter how much of an improvement of the *ZT* level from 1 is achieved, a simple, controllable and highly reproducible thermoelectric material preparation route is urgently needed.

---

[a] *Institute of Physics, Academia Sinica, Nankang, Taipei, Taiwan 11529, R.O.C. E-mail: sankarraman@gate.sinica.edu.tw*

[b] *Centre for Condensed Matter Sciences, National Taiwan University, Taipei 10617, Taiwan. E-mail: fcchou@ntu.edu.tw*

[c] *Institute of Atomic and Molecular Sciences, Academia Sinica, Taipei 10617, Taiwan. E-mail: chenkh@pub.iams.sinica.edu.tw*

[d] *Center of Atomic Initiative for New Materials, National Taiwan University, Taipei 10617, Taiwan*

[e] *Taiwan Semiconductor Research Institute, Hsinchu Science Park, Hsinchu 300, Taiwan, R.O.C*

[f] *Department of Mechanical Engineering, The University of Hong Kong, Pokfulam Road, Hong Kong SAR, China*

† Electronic supplementary information (ESI) available. See DOI: 10.1039/c9ta03503f

Herein, we report a highly reproducible study of germanium telluride (GeTe) as a strong candidate for a high *ZT* thermoelectric material – one which belongs to the same family of the recently reported SnSe[16,19] with a high *ZT* of ~2.6–2.8 at ~773–925 K.[16,19] Many previously mentioned strategies have been tested on GeTe and these were discussed fully by Min Hong *et al.*[20] GeTe is a group IV–VI narrow-band gap semiconductor with a significant divergence in electronic and thermal transport properties, allowing wide spectrum of parameter tuning, which has also been demonstrated and used in a number of applications, including ferroelectrics,[21] rewritable discs,[22] advanced memory devices,[22] and thermoelectrics, due to its fascinating phase-change property with temperature.[21] The highly p-type metallic conductivity behaviour of GeTe has been shown to come from the Ge vacancies, which creates a great opportunity for tuning the carrier concentration *via* control of the vacancy level. Encouraged by the advantages of the low symmetry rhombohedral-phase of GeTe with a high *ZT* reported by Pei *et al.*,[23] the exciting GeTe–$AgSbTe_2$ alloy known as TAGS [tellurium-antimony-germanium-silver] has been widely used by NASA in space missions since 1960.[24] Also, given the limited application of PbTe (*ZT* ~2.5) due to the high toxicity of Pb, GeTe could be the best alternative to achieve a high *ZT* material for practical use in the group of p-type IV–VI narrow-band-gap semiconductors.[25]

The optimization of the carrier concentration n in GeTe has been mostly demonstrated by doping. For example, a simultaneous increase in the power factor and reduction in thermal conductivity through herringbone structures with nano- and meso-scale grain boundaries has been achieved *via* the Sb doping of *ZT* up to 1.85 at 725 K.[23] In addition, a small amount of indium (In) incorporation has been shown to tune the density of states (DOS) at the Fermi level, which raised the peak *ZT* value of 2.3 from 650 K to 780 K.[9] The co-doping of Sb and Pb has also been reported to raise the *ZT* value to 2.3 at 800 K.[26] Many aliovalent dopants, such as Bi,[27] Sb,[10,28] Pb, [29]Cd,[30,31] Mn,[31] In,[10] and Sn,[32] have been applied to explore the impact of carrier doping and crystal symmetry change for GeTe. More similar composite approaches of PbTe-rich and Bi doping of GeTe have also been shown to enhance the *ZT* value to ~2.1 at 700 K.[5] A recent report from Ming Hon *et al.* reported that Cd/Bi co-doped GeTe is able to converge the L and Σ bands by the Cd doping and to reduce the carrier concentration by the Bi doping, which led to an improvement of the *ZT* value up to ~2.2 at 650 K.[11]

It is important to note that all the reported doped GeTe compounds with a high *ZT* also have a high Ge-vacancy level, leading to a high carrier concentration of $\sim 10^{21}\ cm^{-3}$.[20,28] Due to such a high and uncontrolled vacancy level of Ge, the Seebeck coefficient of the bare GeTe has been reported to range from ~30 to $\sim 130\ \mu V\ K^{-1}$ [24,33] at high temperatures. On the other hand, the thermal conductivity of the bare GeTe is $\sim 8\ W\ m^{-1}\ K^{-1}$ at 300 K and $\sim 3.5\ W\ m^{-1}\ K^{-1}$ at 750 K, where a high electronic contribution of the thermal conductivity is unfavourable due to the vacancy-introduced higher carrier concentration.[28,33] In the present study, we successfully fabricated a series of GeTe samples with a controlled vacancy level *in situ* to retain the rhombohedral phase (space group *R*3*m*) without converting to the high-temperature cubic phase (space group $Fm\bar{3}m$) above ~400 °C. Because the initial ratio of Ge : Te was maintained at 1 : 1 and the GeTe was sealed in an evacuated quartz tubing in the process, even though the base material of GeTe prepared at 750 °C had an unavoidable high Ge-vacancy level incorporated in the crystal structure, it was implied that the remaining Ge must exist in the domain boundary or interstitial sites of the rhombohedral phase. In the following annealing process at different temperatures ranging from 800 °C to 900 °C, the excess Ge originally stored in the system was released to refill the Ge-vacancy sites. As a result, a series of vacancy-controlled GeTe samples were prepared *in situ*, *i.e.*, the originally stored Ge in the domain boundaries and interstitial sites was partially released to refill the Ge-vacancy sites of the crystal structure depending on the post-annealing temperature, which was reflected in the significantly increased domain size for the low-Ge-vacancy sample of the various herringbone-structured microdomain patterns. The main advantage of such *in situ* microdomain control for the rhombohedral phase is to raise the Seebeck coefficient and lower the thermal conductivity simultaneously. In particular, the rhombohedral-to-cubic phase transition for the GeTe system near ~400 °C could be suppressed effectively for the nearly Ge-vacancy-free and large herringbone-structured domain sized samples *via* the proposed *in situ* preparation route, which prevented the formation of the high vacancy cubic phase at high temperature, which would otherwise have a detrimental impact on the thermoelectric properties. In addition, such an *in situ* vacancy control process was demonstrated to be reliably reproducible at least three times in our laboratory, which showed its great value in practical applications requiring a nontoxic thermoelectric material with a *ZT* as high as 1.37 at 773 K.

Experimental section

Fabrication of vacancy- and microdomain-controlled GeTe

Material synthesis. Ge and Te metals used as precursors were purchased from Sigma-Aldrich but were purified one more time before use. Starting from the base GeTe sample with a ratio of Ge : Te = 1 : 1, the precursors were sealed in an evacuated quartz tubing and heated at 750 °C for 24 h. The base samples were separated into three batches and resealed in the evacuated quartz tubing to anneal at 800 °C, 850 °C, and 900 °C for 24 h, then labelled as GeTe-800, GeTe-850, and GeTe-900, respectively. We planned our experiments systematically using temperatures in between the melting and boiling points of both chemicals. Our synthesis was carried out in a two-step process as explained in the manuscript, whereby the initial synthesis was done at 750 °C to form the GeTe pure phase with a high level of Ge vacancies. In the post-annealing process at different temperatures of 800 °C, 850 °C, and 900 °C, all the samples were treated below the boiling point (~988 °C) of Te metal and the melting point (~938.2 °C) of Ge. We obtained lower *ZT* values for samples using a post-annealing temperature above 950 °C, which did create more Ge vacancies as expected, but unfortunately this was too close to the boiling point of Te and the sample ended up stabilized in the cubic structure, which prefers to accommodate the most Ge vacancies in a 3D structure. All the samples were air-quenched to room temperature at the end. The collected ingots were then ground into fine powder for 2 h *via* hand-milling and compressed into cylindrical pellets using a graphite die (~15 mm) under a hot press of 50 MPa pressure at 540 °C for 15 min in a high vacuum of $\sim 10^{-6}$ Torr. The densities of the sintered pellets were measured by conventional Archimedes as near ≈98% of the theoretical density.

Phase and microstructure characterization. The phase purity of the as-synthesized powder and pellets were characterized by powder XRD (Bruker D8 diffractometer) equipped with CuK_α radiation ($\lambda = 1.5406$ Å). The phase purity for the hot-pressed GeTe samples was referred to by the powder X-ray diffraction results, as shown in Fig. S(1) (ESI†), and was used in the thermoelectric property measurements. All the prepared samples were confirmed to have the rhombohedral structure, being correctly indexed with the space group $R3m$ at room temperature (RT). The (003) peak position showed a shift towards lower Bragg angles from GeTe-800 to GeTe-900 systematically (inset Fig. S(1)†), which suggested the increase in d-spacing. It was also clear that the Ge and Te atoms were uniformly distributed without the signature of Ge precipitants using FE-SEM, as shown in Fig. S(2).†[26,33] The EDAX analysis suggested that the Ge to Te atomic ratio was close to 1. Additional results from chemical analysis by electron probe microanalysis (EPMA) are tabulated in Table 1, where it can be seen that the Ge content systematically increased with the increasing annealing temperature. DSC profiles were collected using a DSC 404F3 NETZSCH instrument with a heating and cooling rate of 5 K min^{-1} from RT to 500 °C. The elemental compositions were confirmed by EPMA, and the elemental distribution was further confirmed by the FE-SEM micrographs. The structural and chemical characteristics of the sintered pellets were examined with TEM (Philips Tecnai F20, equipped with EDS for compositional analysis).

Computational details. Density functional theory (DFT) calculations were performed using the Vienna *ab initio* simulation package (VASP).[34,35] The generalized gradient approximation (GGA) in the form of Perdew–Burke–Ernzerhof (PBE) parameterization was employed.[36] The effective band structures were computed using Band UP.[37] An energy cutoff of 300 eV was applied and the electronic convergence criterion was set to 1×10^{-5} eV. We applied Γ-centered Monkhorst–Pack k-point meshes[37] of 5 × 7 × 5 for the structural relaxations and 7 × 10 × 7 for the charge self-consistent calculations. Spin-orbit coupling (SOC) was considered in the self-consistent and band structure calculations. A 3 × 2 × 1 super cell containing 36 atoms, which was based on the GeTe $R3m$ conventional cell, was constructed to simulate Ge vacancies. A quasi-random structure of $Ge_{16}Te_{18}$, which contains two Ge vacancies, was constructed using USPEX.[38] For effective band structure calculations, atomic positions were relaxed after inducing Ge vacancies. The electronic density of states was calculated after full optimization of the super cell.

Thermoelectric property measurements. The thermal diffusivity (D) and specific heat (C_p) were measured on sintered pellets (6 mm diameter and thickness of ~2 mm) by a laser flash method (LFA 457, NETZSCH) with reference to pyroceram standard calibration using the Dulong–Petit law, and κ was calculated using $\kappa = DC_p\rho$. Carrier transport studies were performed on a parallelepiped-shaped (3 × 2 × 15 mm^3) cut and polished pellet under He gas atmosphere, with σ and S measured simultaneously on a ZEM-3, ULVAC. The Hall coefficient (R_h) was measured using the PPMS AC transport 5-point probe measurement in a magnetic field of up to 5T. The carrier concentration (n) and mobility (μ) were calculated by using $n = 1/(eR_h)$ and $\mu = \sigma R_h$, where e represents the electron charge.

Results and discussion

Challenges preparing the high-temperature rhombohedral phase of pure GeTe

The pristine GeTe alloy has been demonstrated to show a ZT level peak at a high temperature near ~600 K for ZT ~2.3; however, deterioration occurs above 600 K as a result of the unavoidable rhombohedral-to-cubic phase transition.[23] It is obvious that based on the band picture of the rhombohedral phase of GeTe,[23,25] such an increasing trend of ZT at high temperature should not be limited if the rhombohedral-to-cubic phase transition can be suppressed. However, our nominal GeTe samples prepared in an evacuated sealed tubing environment already suffered from a high Ge-vacancy level, and the rhombohedral-to-cubic phase transition at high temperature became unavoidable, mostly because the high temperature sample of the high Ge-vacancy level prefers the high symmetry cubic phase, which is favourable for accommodating more vacancies in the isotropic distribution. In fact, many reported ultrahigh ZT values for the group IV–VI narrow-band-gap semiconductors at high temperature, including SnSe, SnTe and PbTe,[6,9,13,16,19,39] all are closely related to the phase stability near the phase boundary between the low temperature layered-

Table 1 Elemental analysis and transport properties of GeTe prepared with different post annealing temperatures having various Ge vacancy levels tuned *in situ*

	Atomic ratio, Ge : Te	Carrier conc. (n) ($\times 10^{20}$ cm^{-3})	m^*	Mobility cm^2 V^{-1} S^{-1}	σ (S cm^{-1}) (300/773 K)	S (μV K^{-1}) (300/773 K)	$S^2\sigma$ (μW cm^{-1} K^{-2}) (300/773 K)	κ (W m^{-1} K^{-1}) (300/773 K)	ZT (300/773 K)
GeTe-800	45.03 : 54.97	9.01	1.72	45.03	6494/2936	39/107	10.2/34	5.87/3.70	0.05/0.70
GeTe-850	47.40 : 52.60	7.97	1.35	60.84	7669/1704	34/167	8.78/46.5	7.73/2.97	0.03/1.23
GeTe-900	49.95 : 50.05	7.33	1.28	70.54	8228/1811	33/161	8.94/47.5	7.04/2.62	0.04/1.37

like (or rhombohedral distortion) structure and the high symmetry 3D structure without a controlled vacancy level. It is clearly desirable to prepare stable group IV–VI narrow-band-gap semiconductor samples near the pseudo-cubic-to-cubic phase transition, but keep the pseudo-cubic-phase-stability temperature as high as possible, so that the thermoelectric materials can be operated in a high temperature environment efficiently.

In the preparation of the GeTe sample targeted at a high *ZT* thermoelectric performance at high temperature, two factors are unfavourable but difficult to avoid: the first is the high Ge-vacancy level generated as a result of the low melting point and high vapour pressure,[33] and the second is the rhombohedral-to-cubic phase transition near ~400 °C, mostly because the cubic phase is preferred to incorporate more vacancies and to stabilize the structure at high temperature.[40] In the present investigation, we designed an *in situ* Ge-vacancy control route to suppress the unfavourable rhombohedral-to-cubic phase transition near ~400 °C, *i.e.* a near vacancy-free rhombohedral phase of GeTe has been prepared. It was more surprising to find that the nearly vacancy-free rhombohedral phase had a large microdomain size in the herringbone structure also, which provides an additional beneficial factor to reduce the phonon contribution to thermal conductivity across the domain boundaries. As a result, the combination of the increased Seebeck coefficient and lowered thermal conductivity was able to enhance *ZT* value to as high as 1.37 at ~500 °C. Most importantly, the newly designed preparation method did not involve doping or even co-doping,[3,23] and was highly reproducible *via* an *in situ* vacancy control route, which was confirmed more than three times reproducibly in our lab from the pure element precursors.

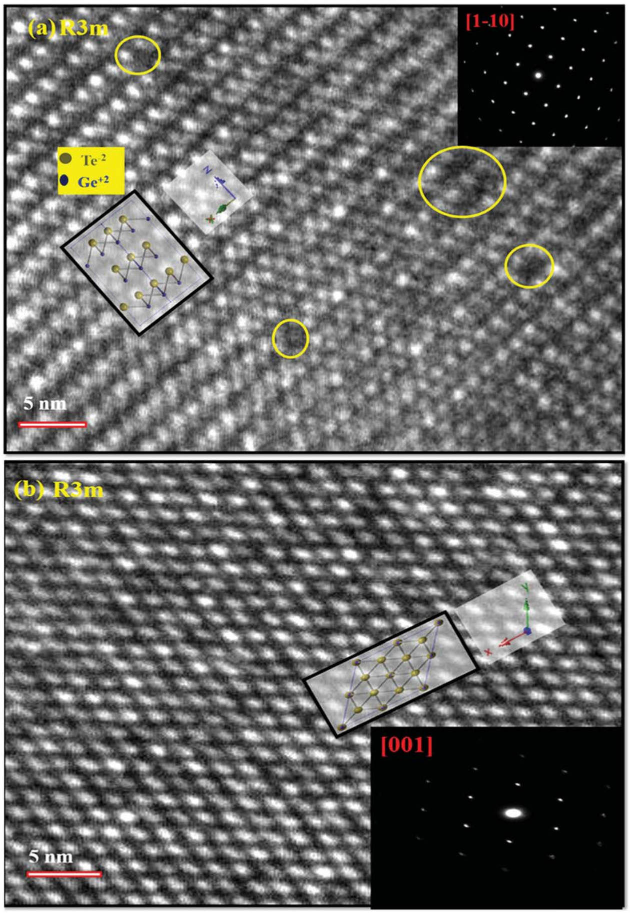

Fig. 1 Atomic and diffraction patterns of the GeTe-800 sample in the rhombohedral symmetry of space group $R3m$. (a) TEM and SAED patterns (inset) taken along the [1$\bar{1}$0] direction, and (b) along the [001] direction. The corresponding crystal projection is overlaid to show the correct lattice size and atomic arrangement.

Herringbone-structured microdomains of GeTe

GeTe has a rhombohedral structure of the space group $R3m$ at room temperature (RT), but a structural phase transition occurs near ~400 °C and transforms it into a NaCl-type cubic structure of space group $Fm\bar{3}m$.[40] For the rhombohedral phase in a hexagonal representation, each close packing (001) plane of GeTe corresponds to the (111) plane of a cubic phase. A slightly distorted lattice of $a = 5.98$ Å with a small angle deviation of $\alpha = 88.35°$ from the expected 90° has been implied from the structure refinement before,[33,41] which is consistent with the averaged local distortion due to severe Ge vacancies and interstitials.[41] Fig. 1(a) reveals the HR-TEM pattern for the rhombohedral phase of GeTe-800 taken along the [1$\bar{1}$0] direction, where a nonuniform distance between two successive (*hk*0) planes and areas of darker contrast are identifiable,[17,41–43] presumably as a result of both the Ge vacancy and the interstitial Ge existence between layers. The selected area electron diffraction (SAED) pattern shown in the inset clearly demonstrates the crystallinity of the rhombohedral phase along the [1$\bar{1}$0] direction for the GeTe-800 sample. Fig. 1(b) shows the HR-TEM pattern for the GeTe-800 sample taken along the [001] direction, which shows the expected hexagonal symmetry for the (001) plane of $R3m$, as also confirmed by the SAED diffraction pattern shown in the inset.

It is well known that GeTe forms a herringbone structure of microdomains in its rhombohedral phase. There are several types of different preferred orientations of the rhombohedral axis, mostly seen along the [1$\bar{1}$0] projection in the herringbone structure, and domains of the preferred orientation show a systematic arrangement by the different contrast.[41,43] Fig. 2 shows the TEM microstructural analysis of the GeTe-800 and GeTe-900 samples. The microdomain structures for GeTe-800 with more Ge vacancies are shown in Fig. 2(a)–(c), where many herringbone-structured microdomains can be observed with a small column separation. The magnified domain structures of GeTe -800 revealed a small domain size of ~10 nm with irregular domain boundaries, which is consistent with the higher Ge-vacancy level within the domains and the existence of interstitial Ge near the domain boundaries. On the other hand, GeTe-900 nearly free of Ge vacancies (see Table 1) showed a similar herringbone structure but a much larger domain size with well-defined domain boundaries up to ~200 nm, including a twin domain and inverse domain boundary, which is consistent with the picture showing that more clean domain boundaries are formed for GeTe-900 when the excess Ge originally stored in the interstitial sites is moved into the Ge-vacancy sites after higher temperature annealing.[13,43] Several more domain structure patterns for GeTe-900 are shown

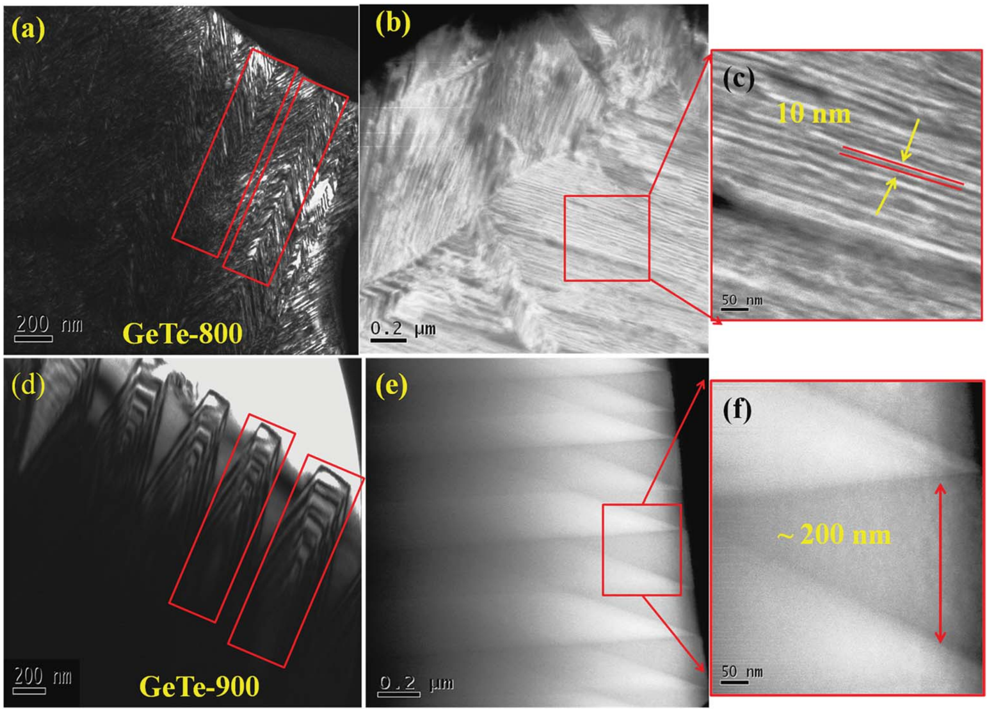

Fig. 2 HR-TEM pictures to show the microdomain structural changes of GeTe having various Ge vacancy levels. (a) GeTe-800 with more Ge vacancies and high density herringbone-structured microdomains, (b) magnified view, and (c) zoom in to show the narrow domains of ~10 nm for GeTe-800. (d) GeTe-900 with less Ge vacancies and a low density larger microdomain size, (e) magnified view of the near domain boundaries, and (f) zoom in to see the varying sizes of inverse domains for the domains up to ~200 nm for GeTe-900.

in the ESI† [Fig. S(3)], including the parallel domains of the preferred orientation and twin domains, consistent with the rhombohedral nature of the crystal symmetry. These domains of different lengths and angles may create more phonon scattering, which reduces the thermal conduction.[28]

Temperature-dependent TEM analysis

Prior to performing the high-temperature TEM phase change analysis, we analysed the samples through differential scanning calorimetry (DSC) studies. The DSC studies were conducted by using ~60 mg of GeTe samples between RT and 500 °C with a heating/cooling rate of 5 °C min^{-1} under an argon gas atmosphere, as shown in Fig. 3. Small endothermic and exothermic peaks could be observed for the GeTe-800 sample upon heating and cooling with onsets near ~350 °C and ~310 °C, respectively, where this temperature corresponds to the structural phase transition for GeTe-800 being converted from the rhombohedral symmetry ($R3m$) to the cubic symmetry ($Fm\bar{3}m$).[22,41] It is interesting to note the large difference between the onsets of melting and solidification, which is consistent with the irreversible domain boundary formation observed in the TEM analysis. Even without considering the parameter of the vacancies, the structural phase transition for GeTe has been predicted to be fluctuation-driven and of a first-order type theoretically.[40] To scrutinize the evolution of the microdomain structure with temperature, we performed high-temperature TEM experiments. Fig. 3 shows the temperature evolution of the phase and microdomain variations for GeTe-800. It could be

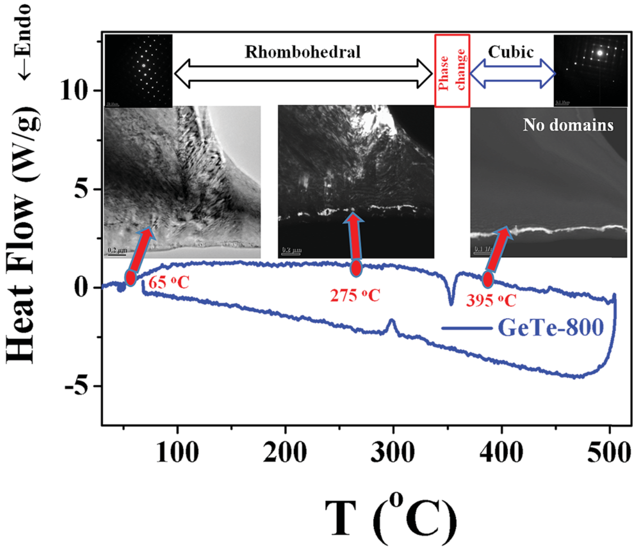

Fig. 3 Differential scanning calorimetry study and corresponding domain structure pictures for GeTe-800 with more Ge vacancies and high density herringbone microdomain structures. The DSC scan shows clear exothermic (endothermic) reactions of onsets near ~350 °C (~310 °C) to indicate the structural phase transition. The thermal hysteretic behaviour supports the domain existence due to the irreversible domain formation. The corresponding TEM pictures show the domain structure at temperatures above and below the phase transition. The domain structure disappears above ~395 °C, indicating the highly symmetric cubic phase transformation. Top insets reveal the SAED patterns of rhombohedral and cubic symmetries.

seen that the microdomains had merged systematically to form a highly symmetric cubic ($Fm\bar{3}m$) phase at ∼395 °C, which is consistent with the DSC study results. Further SAED analysis at elevated temperatures aided the postulation that the domain disappearance was due to its high symmetry.[43]

Fig. 4 shows both warming and cooling curves for the DSC scans and high-temperature TEM pictures for GeTe-900 nearly free of Ge vacancies and with large herringbone-structured microdomains. Surprisingly, no endothermic and exothermic peaks were observed for GeTe-900, which suggests that GeTe-900 maintained its RT rhombohedral symmetry up to ∼500 °C without converting to the cubic symmetry reversibly. The herringbone structure of GeTe-900 at room temperature could be seen to deviate from its regular arrangement with increasing temperature, until the main domain type was missing as a result of the partially relieved strain *via* thermal fluctuation, while the narrow and high density herringbone-structured domains remained stable up to 455 °C. On the cooling down scan, the herringbone structure of the microdomains was recovered nearly reversibly but lost contrast and size. It is proposed that the domain size change after thermal cycling is due to the relief of the strain energy through systematic domain boundary formation, and this energy transfer allows bypassing the storage of latent heat, which is required for the first-order structural phase transition. The high-temperature rhombohedral structural stability of the GeTe-900 was confirmed with temperature-dependent synchrotron X-ray diffraction also, as shown in Fig. 5. The peak doublet for 2θ between 41–45° revealed a rhombohedral symmetry nature, which was confirmed by the indexing of the (024) and (220) planes in the $R3m$ space group. It is clear that the rhombohedral phase was maintained throughout the temperature range up to 500 °C without the appearance of a Bragg peak for the cubic phase.[26,28,30] A small shift in peaks was observed systematically due to lattice strain change for the samples with a microstructure, which is consistent to that concluded in the microdomain structure evolution in the TEM pictures (Fig. 4).

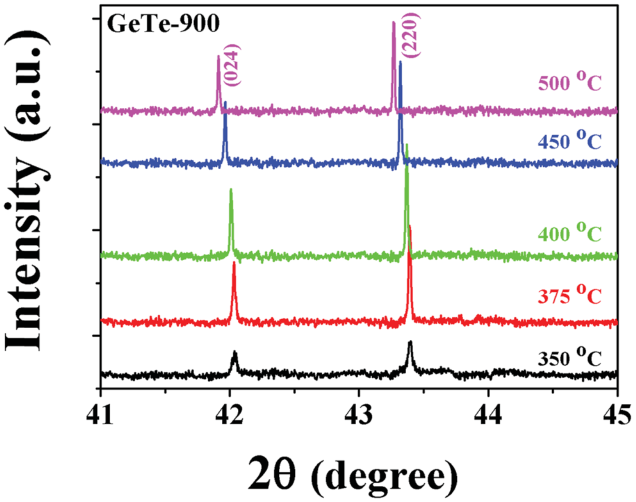

Fig. 5 Temperature dependence of the synchrotron X-ray diffraction patterns for GeTe-900 indexed with the (024) and (220) planes using the $R3m$ space group, which shows no peak emerging between 2θ ∼41–45°, *i.e.* no rhombohedral-to-cubic phase transition was identified above RT and up to 500 °C.

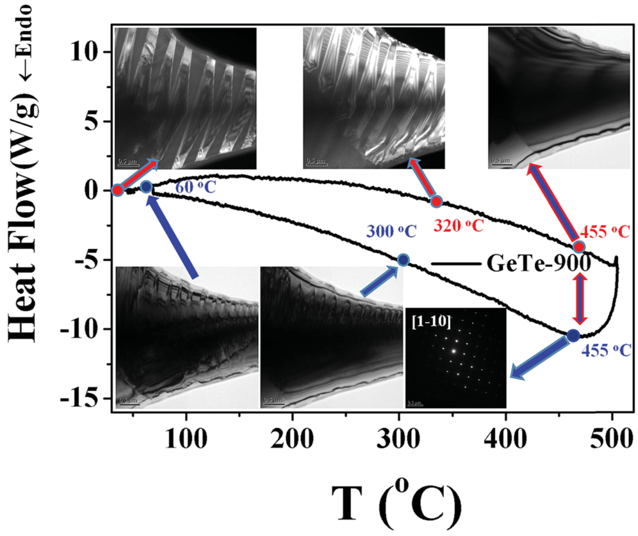

Fig. 4 Differential scanning calorimetry study and corresponding TEM pictures for the domain structure of GeTe-900 nearly free of Ge vacancies and large herringbone-structured domain sizes. No clear exothermic or endothermic peaks were found below 500 °C. TEM pictures suggest small domains remain along the [1$\bar{1}$0] plane of the $R3m$ space group up to 455 °C. A reversible domain formation is observed upon cooling but of relatively lower contrast.

Vacancy-dependent calculations of the band structure

To examine the effect of Ge vacancies on the electronic band structure of GeTe, we applied density functional theory (DFT) calculations with spin orbital coupling (SOC) by using the Vienna *ab initio* simulation package (VASP) for the pristine sample and the samples of different Ge vacancies. Fig. 6 shows the calculated band structures for $Ge_{18}Te_{18}$, $Ge_{17}Te_{18}$ and $Ge_{16}Te_{18}$, where the impact of the Ge-vacancy level on the rhombohedral GeTe was revealed by the evolution of the valence band maximum (VBM) and conduction band minimum (CBM). The Fermi level of $Ge_{18}Te_{18}$ lay almost at top of the valence band, whereas it moved toward the valence band with the increasing effective mass (m^*) for $Ge_{17}Te_{18}$ and $Ge_{16}Te_{18}$ progressively.[44] Fig. 6(d) shows that the total DOS at the Fermi level moved down for higher Ge-vacancy levels, which is in agreement with the enhancement of charge carriers due to the increasing Ge vacancies for $Ge_{17}Te_{18}$ and $Ge_{16}Te_{18}$. Fig. S(4) in the ESI† shows the detailed DOS calculations for Ge and Te states separately, which suggests that for samples with Ge vacancies, the DOS in the valence band will be dominated by Te-5p^4 and Ge-4s^2 orbitals, whereas the Ge-4p^2 orbital will dominate the conduction band minima in the conduction band.

Thermoelectric properties

The thermoelectric properties for GeTe samples with a controlled Ge-vacancy level and microdomain structure as a function of temperature are summarized in Fig. 7, including the electrical conductivity (σ), Seebeck coefficient (S) and

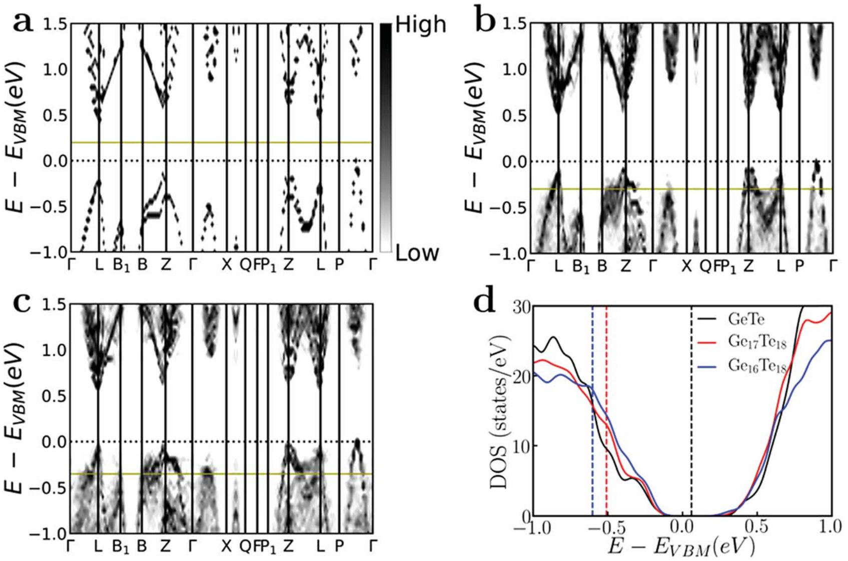

Fig. 6 The calculated effective band structures for (a) the pristine GeTe, (b) $Ge_{17}Te_{18}$ with an intermediate Ge vacancy level, and (c) $Ge_{16}Te_{18}$ with a higher Ge vacancy level. The valence band maximum is shifted to 0 eV and highlighted by horizontal dash lines. Fermi level is denoted by yellow solid lines. (d) Density of states of GeTe, $Ge_{17}Te_{18}$ and $Ge_{16}Te_{18}$, with Fermi levels indicated by the vertical dashed lines.

thermal conductivity (κ). Several general trends could be observed and can be explained due to the dependence on the temperature and microdomains. First, for the measured electrical conductivity shown in Fig. 7(a), σ lowers with increasing the temperature for all samples (from GeTe-750 to GeTe-900) with various microdomain densities and sizes, which is a typical electrical conducting behaviour for GeTe as a narrow-band-gap semiconductor. Second, even though GeTe-750 was expected to have a higher carrier concentration due to having more Ge vacancies, the trend of increasing σ from GeTe-750 to GeTe-900 at RT reflects the impact of scattering from the domain boundaries, *i.e.* the higher density of microdomains for GeTe-750 introduced significant scattering to reduce the effective mobility, which is responsible for the lowest electrical conductivity at RT. Third, a significant step in increase could be identified for GeTe-750 and GeTe-800 across the temperature range for the rhombohedral-cubic structural phase transition near ~400 °C, which implies that the shrunk defect-type cubic phase (see Fig. 3) would allow the accommodation of more vacancies which is responsible for the significantly enhanced electrical conductivity.[10,31]

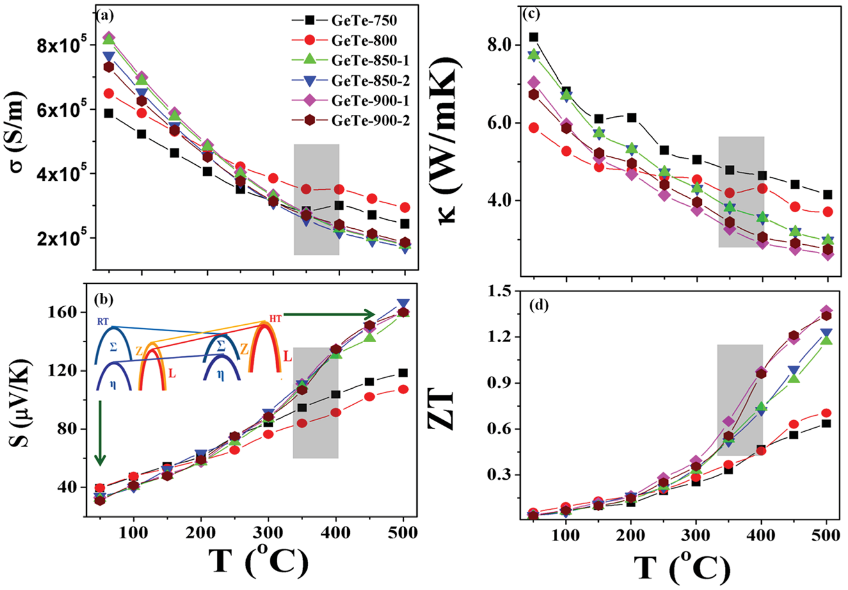

Fig. 7 Temperature dependence for GeTe of various Ge vacancy levels and microdomain structures, (a) electrical conductivity, (b) Seebeck coefficient, (c) thermal conductivity, and (d) *ZT* (The expected temperature range of the rhombohedral-cubic phase transformation is highlighted with the grey block).

The temperature dependence of the Seebeck coefficients for the GeTe system is shown in Fig. 7(b). The Seebeck coefficients for the series of GeTe samples were p-type and were confirmed by the positive Hall measurement. The Seebeck coefficients for all the samples showed a similar trend of increase with increasing temperature. There was no significant impact of the Ge-vacancy level on the Seebeck coefficient at RT from GeTe-800 to GeTe-900. On the other hand, a significant enhancement of the Seebeck coefficient for GeTe-850 and GeTe-900 at HT was observed, especially above the temperature range of ~400 °C for the expected rhombohedral-to-cubic structural phase transition, but this was suppressed for GeTe-900 (see Fig. 4). The significant enhancement of the Seebeck coefficient for GeTe-900 (~47.6 μW cm^{-1} K^{-2}) led to the highest power factor for the polycrystalline hot-pressed samples of pure GeTe without doping. We tested the experimental results for the current thermoelectric properties more than three times starting from the same precursors, as presented in the ESI† in Fig. S(5), which clearly confirmed the identical thermoelectric properties for the samples prepared by the same route.

The significant enhancement of the Seebeck coefficient (S) for GeTe-900 can be explained based on the tuning of three major parameters of S, namely the temperature T, effective mass m^* near the Fermi level, and the carrier density n near the Fermi level, *i.e.* $S \sim T\ (m^*\ 1/n^{2/3})|_{E_f}$.[3,4] For the rhombohedral GeTe without vacancies, the band picture evolution from RT to HT has been proposed,[23] in contrast to the band picture evolution for the cubic phase.[3] Schematic plots for the RT and HT bands of vacancy-free GeTe-900 are shown in the inset of Fig. 7(b). It is clear that as long as the cubic phase is suppressed for GeTe-900 at 500 °C, the convergence of the L and Σ bands at elevated temperatures would favour the increasing m^* as a result of both contributions from the converged L and Σ bands from the heavier effective mass near the Fermi level.[20,23,28] By combining all the favourable factors, including the higher temperature, the heavier m^* near the Fermi level, and the reduced carrier density for GeTe-900, it is not surprising to find GeTe-900 achieved the highest Seebeck coefficient of S ~47.6 μW cm^{-1} K^{-2} at 500 °C.[25,28,30] The temperature-dependent power factor for the GeTe samples of different vacancy levels is shown in Fig. S7(a).†

Thermal conductivity as a function of temperature for the GeTe system is shown in Fig. 7(c). The decreasing κ as a function of increasing temperature for all the samples is consistent with the picture that the increasing thermal fluctuation reduces the dominant phonon-assisted energy transport. GeTe-750 with the most Ge vacancies could be expected to show a stronger electronic contribution of κ (κ_{ele}), which was consistent with its highest total thermal conductivity of ~4.15 W m^{-1} K^{-1} near 500 °C. On the other hand, GeTe-900 with the lowest Ge-vacancy level had the lowest total thermal conductivity at 500 °C, which could be explained due to both the lowered κ_{ele} as a result of carrier density reduction for the vacancy-free domains and the lowered κ_{lat} due to the significantly increased phonon scattering across the domain boundaries. As shown in Fig. S(3) and S(6) in the ESI,† various lengths from ~0 nm to ~200 nm of the inverse domain type could be observed, which must create barriers for phonon-assisted thermal flow transport crossing the domain boundaries of various sizes, orientations and shapes.[12,13] A detailed lattice and electronic contribution to the thermal conductivity was plotted and shown in the ESI† (Fig. S7(b)), where the electronic thermal conductivity was calculated using the Weidman Franz law ($\kappa_{\text{ele}} = L\sigma T$).[1,2,15]

Fig. 7(d) summarizes the thermoelectric performance (ZT) of the GeTe system. With the optimization of the thermoelectric properties *via* Ge vacancy and microdomain structure control, it is clear that the GeTe-900 sample achieved a ZT of ~1.37 at 500 °C. This enhancement was about 58% higher than those reported values for GeTe to date.[25,26,29,30,43] In particular, the current preparation method for the Ge vacancy and microdomain structure control was confirmed to be reliably reproducible and without the involvement of doping, which could otherwise introduce uncontrollable factors, like local strain and impurity phases. These results must energize the performance of GeTe-based thermoelectric materials with more controllable stability with less complications than from the substitution route.

Conclusions

In this investigation, we propose a highly reproducible route for the preparation of nearly Ge-vacancy-free rhombohedral phase of GeTe to show a ZT of ~1.37 at 500 °C. The *in situ* Ge-vacancy control route was able to suppress the commonly found rhombohedral-to-cubic phase transition that loses the favourable band picture for rhombohedral symmetry with a high effective mass near the Fermi level, which allows both an increase in the Seebeck coefficient and a reduction of the thermal conductivity simultaneously up to 500 °C. The vacancy-free rhombohedral phase was shown to have a large microdomain size in a herringbone structure, which provides an additional scattering mechanism to reduce the phonon contribution of thermal conductivity through scattering across domain boundaries of different crystal orientations and allows limited correlation lengths for the transport of thermal flow *via* phonons of selected wavelengths. Most importantly, the newly designed preparation method does not involve doping, which could otherwise complicate the data interpretation and sample quality control, and further, our method is highly reproducible *via* an *in situ* vacancy control route, which was confirmed with a more than three times reproducibility starting from the pure element precursors. The current strategy of sample preparation may apply to most group IV–VI narrow-band-gap semiconductors with known structural phase transition, and the newly identified vacancy–domain correlation provides an unambiguous interpretation to the Seebeck coefficient that relies heavily on the band picture calculations.

Conflicts of interest

The authors declare no conflict of interest.

Acknowledgements

Sankar Raman acknowledges the project grant towards the thermoelectric material for sustainable energy project: AS-SS-

106-01-1. The authors are thankful to Taiwan Photon Source (TPS) situated at the National Synchrotron Radiation Research Center (NSRRC) for studying temperature dependent synchrotron X-ray diffraction (XRD) data. FCC acknowledges the support provided by the Ministry of Science and Technology in Taiwan under project number MOST-106-2119-M-002 -035 -MY3. Financial support by the Center of Atomic Initiative for New Materials, National Taiwan University, from the Featured Areas Research Center Program within the framework of the Higher Education Sprout Project by the Ministry of Education in Taiwan (108L9008), is acknowledged. CX and YC are grateful for the financial support from Zhejiang Provincial Natural Science Foundation under project number LR19A040001, and the research computing facilities offered by ITS, HKU.

References

1 S. Roychowdhury, M. Samanta, S. Perumal and K. Biswas, *Chem. Mater.*, 2018, **30**, 5799–5813.

2 M. Samanta, S. Roychowdhury, J. Ghatak, S. Perumal and K. Biswas, *Chem. – Eur. J.*, 2017, **23**, 7438–7443.

3 Y. Pei, X. Shi, A. LaLonde, H. Wang, L. Chen and G. J. Snyder, *Nature*, 2011, **473**, 66.

4 W. Liu, X. Tan, K. Yin, H. Liu, X. Tang, J. Shi, Q. Zhang and C. Uher, *Phys. Rev. Lett.*, 2012, **108**, 166601.

5 L. Zhao, H. Wu, S. Hao, C.-I. Wu, X. Zhou, K. Biswas, J. He, T. P. Hogan, C. Uher and C. Wolverton, *Energy Environ. Sci.*, 2013, **6**, 3346–3355.

6 A. Banik, U. S. Shenoy, S. Anand, U. V. Waghmare and K. Biswas, *Chem. Mater.*, 2015, **27**, 581–587.

7 S. V. Faleev and F. Léonard, *Phys. Rev. B*, 2008, **77**, 214304.

8 B. Khasimsaheb, S. Neeleshwar, M. Srikanth, S. Bathula, B. Gahtori, A. K. Srivsatava, A. Dhar, A. Sankarakumar, B. K. Panigrahi and S. Bhattacharya, *J. Mater. Res.*, 2015, **30**, 2638–2648.

9 J. P. Heremans, V. Jovovic, E. S. Toberer, A. Saramat, K. Kurosaki, A. Charoenphakdee, S. Yamanaka and G. J. Snyder, *Science*, 2008, **321**, 554–557.

10 M. Hong, Z. G. Chen, L. Yang, Y. C. Zou, M. S. Dargusch, H. Wang and J. Zou, *Adv. Mater.*, 2018, **30**, 1705942.

11 L. Hicks and M. Dresselhaus, *MRS Online Proc. Libr.*, 1993, 326.

12 K. Biswas, J. He, Q. Zhang, G. Wang, C. Uher, V. P. Dravid and M. G. Kanatzidis, *Nat. Chem.*, 2011, **3**, 160.

13 K. Biswas, J. He, I. D. Blum, C.-I. Wu, T. P. Hogan, D. N. Seidman, V. P. Dravid and M. G. Kanatzidis, *Nature*, 2012, **489**, 414.

14 L.-D. Zhao, S. Hao, S.-H. Lo, C.-I. Wu, X. Zhou, Y. Lee, H. Li, K. Biswas, T. P. Hogan and C. Uher, *J. Am. Chem. Soc.*, 2013, **135**, 7364–7370.

15 M. Samanta and K. Biswas, *J. Am. Chem. Soc.*, 2017, **139**, 9382–9391.

16 L.-D. Zhao, S.-H. Lo, Y. Zhang, H. Sun, G. Tan, C. Uher, C. Wolverton, V. P. Dravid and M. G. Kanatzidis, *Nature*, 2014, **508**, 373.

17 X. Shi, J. Yang, J. R. Salvador, M. Chi, J. Y. Cho, H. Wang, S. Bai, J. Yang, W. Zhang and L. Chen, *J. Am. Chem. Soc.*, 2011, **133**, 7837–7846.

18 R. Venkatasubramanian, E. Siivola, T. Colpitts and B. O'quinn, *Nature*, 2001, **413**, 597.

19 L.-D. Zhao, G. Tan, S. Hao, J. He, Y. Pei, H. Chi, H. Wang, S. Gong, H. Xu and V. P. Dravid, *Science*, 2015, aad3749.

20 M. Hong, J. Zou and Z. G. Chen, *Adv. Mater.*, 2019, 1807071.

21 M. Wuttig, D. Lüsebrink, D. Wamwangi, W. Wełnic, M. Gilleßen and R. Dronskowski, *Nat. Mater.*, 2007, **6**, 122.

22 H. F. Hamann, M. O'Boyle, Y. C. Martin, M. Rooks and H. K. Wickramasinghe, *Nat. Mater.*, 2006, **5**, 383.

23 J. Li, X. Zhang, Z. Chen, S. Lin, W. Li, J. Shen, I. T. Witting, A. Faghaninia, Y. Chen and A. Jain, *Joule*, 2018, **2**, 976–987.

24 S. Roychowdhury and K. Biswas, *Chem*, 2018, **4**, 939–942.

25 J. Li, Z. Chen, X. Zhang, Y. Sun, J. Yang and Y. Pei, *NPG Asia Mater.*, 2017, **9**, e353.

26 X. Zhang, J. Li, X. Wang, Z. Chen, J. Mao, Y. Chen and Y. Pei, *J. Am. Chem. Soc.*, 2018, **140**(46), 15883–15888.

27 S. Perumal, S. Roychowdhury and K. Biswas, *Inorg. Chem. Front.*, 2016, **3**, 125–132.

28 S. Perumal, S. Roychowdhury, D. S. Negi, R. Datta and K. Biswas, *Chem. Mater.*, 2015, **27**, 7171–7178.

29 Y. Gelbstein, J. Davidow, S. N. Girard, D. Y. Chung and M. Kanatzidis, *Adv. Energy Mater.*, 2013, **3**, 815–820.

30 M. Hong, Y. Wang, W. Liu, S. Matsumura, H. Wang, J. Zou and Z. G. Chen, *Adv. Energy Mater.*, 2018, 1801837.

31 J. Lee, M. Oh, B. Kim, B. Min, H. Lee and S. Park, *Electron. Mater. Lett.*, 2014, **10**, 813–817.

32 L. Neudert, S. Schwarzmüller, M. Scheel, S. Welzmiller and O. Oeckler, *Z. Anorg. Allg. Chem.*, 2017, **643**, 1962–1970.

33 E. Levin, M. Besser and R. Hanus, *J. Appl. Phys.*, 2013, **114**, 083713.

34 M. C. Payne, M. P. Teter, D. C. Allan, T. Arias and a. J. Joannopoulos, *Rev. Mod. Phys.*, 1992, **64**, 1045.

35 G. Kresse and J. Furthmüller, *Comput. Mater. Sci.*, 1996, **6**, 15–50.

36 P. E. Blöchl, *Phys. Rev. B*, 1994, **50**, 17953.

37 P. V. Medeiros, S. Stafström and J. Björk, *Phys. Rev. B*, 2014, **89**, 041407.

38 C. W. Glass, A. R. Oganov and N. Hansen, *Comput. Phys. Commun.*, 2006, **175**, 713–720.

39 C. Chang, M. Wu, D. He, Y. Pei, C.-F. Wu, X. Wu, H. Yu, F. Zhu, K. Wang, Y. Chen, L. Huang, J.-F. Li, J. He and L.-D. Zhao, *Science*, 2018, **360**, 778–783.

40 M. Sist, H. Kasai, E. M. Hedegaard and B. B. Iversen, *Phys. Rev. B*, 2018, **97**, 094116.

41 T. Chattopadhyay and J. Boucherle, *J. Phys. C: Solid State Phys.*, 1987, **20**, 1431.

42 M. Snykers, P. Delavignette and S. Amelinckx, *Mater. Res. Bull.*, 1972, **7**, 831–839.

43 H. S. Lee, B.-S. Kim, C.-W. Cho, M.-W. Oh, B.-K. Min, S.-D. Park and H.-W. Lee, *Acta Mater.*, 2015, **91**, 83–90.

44 B. Srinivasan, R. Gautier, F. Gucci, B. Fontaine, J.-F. Halet, F. Cheviré, C. Boussard-Plédel, M. J. Reece and B. Bureau, *J. Phys. Chem. C*, 2017, **122**, 227–235.